Journal of Molecular Liquids 354 (2022) 118834

Contents lists available at ScienceDirect

Journal of Molecular Liquids

journal homepage: www.elsevier.com/locate/molliq

Mechanical properties of particle-covered droplets probed by nonuniform electric field

Khobaib Khobaib [a,*], Zbigniew Rozynek [a,b], Tomasz Hornowski [a]

[a] Faculty of Physics, Adam Mickiewicz University, Uniwersytetu Poznańskiego 2, 61-614 Poznań, Poland
[b] PoreLab, The Njord Centre, Department of Physics, University of Oslo, Blindern, N-0316 Oslo, Norway

ARTICLE INFO

Article history:
Received 27 October 2021
Revised 6 February 2022
Accepted 25 February 2022
Available online 2 March 2022

Keywords:
Pickering droplet
Nonuniform E-field
Droplet deformation
Electrohydrodynamic flow
PIV analysis
Electrode geometry

ABSTRACT

Particle-covered droplets are used in several fundamental studies and practical applications. For many applications, it is important to understand the mechanics of these droplets subjected to induced external stresses, such as an electric field (*E*-field). Several research groups have studied the deformation and stability of droplets subjected to uniform *E*-fields. However, the behavior of particle-laden droplets in nonuniform *E*-fields is inadequately reported. In this study, we present the deformation of silicone oil droplets coated by an electrically insulating particle shell suspended in castor oil. Such droplets deform compressively under a direct current *E*-field. We create *E*-fields with different intensities and field gradients by changing the applied electric potential, the shape of a signal electrode, and its position relative to a stationary plate-shaped electrode. The experimental results of the droplet deformation are compared with the calculated values obtained through modeling the distribution of a nonuniform *E*-field around a cylindrical electrode using the finite element method. We quantitatively present how the electrode geometry, electric potential, and droplet size affect the magnitude of droplet deformation. Then we relate droplet deformation to the size of an opening in the particle shell created in the presence of an *E*-field. We show that this allows designing procedures for inserting a material into a droplet, as well as inspecting of the interior content of a particle-covered droplet without affecting its particle shell. Furthermore, we study the origin of liquid flows in the sample cell through two-dimensional time-averaged flow maps, finding that the *E*-field-induced flows have two origins. These findings may be relevant for heat-transfer enhancement.

1. Introduction

Understanding the mechanical and rheological properties of droplets (pure or particle-covered droplets) subjected to external stresses is crucial for many practical applications, including the fabrication of emulsions [1–3]. One of the frequently studied parameters, droplet deformation, is essential for various industrial applications, such as inkjet printing [4], droplet separation in microfluidic systems [5], de-emulsification [6,7], biological cell systems [8], and enhanced oil recovery [9]. Several studies have investigated the characteristic of pure droplets under stress. However, particle-covered droplets are a subject of fundamental studies because droplets with a particle shell are important for technological applications such as food products [10], pharmaceutical products [11], cosmetics [12], biocatalysts [13], cell printing [14], biodiesel production [15], drug delivery [16,17], and environmental remediation [18].

Typically, the mechanical and rheological properties of droplets are investigated using mechanical compression [19–21], hydrodynamic shear flow [22,23], or magnetic [24] and electric fields (*E*-fields) [25]. Approaches involving *E*-field have proven to be useful as a noncontact method for studying the response of droplets subjected to an external stress [25–29]. Typically, a uniform *E*-field is used to generate electric stress. Thus, many studies on droplets subjected to a uniform *E*-field have been published [26,30–33].

The use of non-uniform *E*-fields for studying deformation and other characteristics droplets is inadequately reported, which includes the following contributions: Yao *et al.* [34] and Song *et al.* [35] experimentally and theoretically studied the deformation and migration of a leaky dielectric droplet subjected to a steady nonuniform *E*-field; Mhatre *et al.* [36] studied the cyclic motion and deformation of a conductive droplet under a nonuniform *E*-field; Feng [37] provided a theoretical basis for the motion of a deformable fluid particle under a nonuniform *E*-field; Desh-

* Corresponding author.
E-mail address: khokho@amu.edu.pl (K. Khobaib).

https://doi.org/10.1016/j.molliq.2022.118834
0167-7322/

mukh and Thaokar [38] studied the deformation and breakup of a leaky dielectric droplet in a leaky dielectric fluid (under an axisymmetric quadrupole *E*-field); and Ahn *et al.* [39] investigated the role of electrode geometry on droplet-charging characteristics. Our aim is to fill the gaps in this research area by demonstrating how electrode geometry affects the following: (i) the magnitude of droplet deformation; (ii) particle organization within the particle shell; and (iii) the velocity of *E*-field-induced fluid flow in a sample cell.

1.1. Droplet deformation

In silicone oil–castor oil systems (as studied here), a direct current (DC) *E*-field can be used to generate electric stresses that either compress or stretch a droplet depending on the physical parameters of the particles (e.g., dielectric properties, electrical conductivity, and particle size). For example, a silicone oil droplet covered by polyethylene (PE) microparticles deforms compressively, whereas the same droplet covered by Ag-coated silica particles stretches when subjected to a DC *E*-field [27]. In this study, we investigate a three-phase system comprising electrically insulating microparticles. In this system, the electric stress compresses the droplet, which eventually acquires an oblate geometry where the longest droplet axis is perpendicular to the applied *E*-field. We focus on the effects of electrode size, droplet size, and spacing between the electrodes on the magnitude of the oblate deformation of the droplet. In our experiments, we used top electrodes of different shapes and sizes, whereas the bottom plate electrode remained the same for all experiments. The experimental data were compared with results obtained through finite element analysis.

1.2. Particle-shell opening

When a droplet deforms, its surface area increases. In the case of the particle-covered droplet studied herein, the increased surface area causes the unjamming of particles in the shell and the formation of a particle-free area [40]. The size of the opening in the particle shell is directly associated with the magnitude of droplet deformation and can be easily controlled. The ability of a particle shell (formed on a droplet) to be reversibly opened and closed under the action of an *E*-field can be exploited, for example, to form a miniaturized optical diaphragm with an adjustable aperture, to buckle armored droplets, to fabricate droplets with Janus and patchy shells by manipulating the droplet liquid [29], or to unarmor a droplet to enable coalescence [41]. Herein, we will demonstrate how to insert a material into a particle-covered droplet and inspect the interior content of the particle-covered droplet without affecting the particle shell.

1.3. Electrohydrodynamic (EHD) flows

Droplet deformation is accompanied by the induction of EHD flows. In the plate–plate electrode configuration (uniform *E*-field), these EHD flows are strong near the droplet surface [42–44] and they originate from the jump in the tangential component of the electric stress (i.e., circulating flows are formed to compensate for the difference in tangential stress caused by the hydrodynamic stress). For a droplet subjected to nonaxisymmetric *E*-fields, the velocity fields of the circulating flows can be different from those observed for a droplet exposed to an axisymmetric *E*-field [45]. There are other electric mechanisms for generating the convective motion of a fluid in the sample cell (not associated with the charging of the droplet interface). For instance, liquid flows can be induced through ion injection at the metal–liquid interface [46]. In this study, we use particle image velocimetry (PIV) experiments to generate two-dimensional time-averaged flow maps to study the origin of the flows in the sample cell and investigate the influence of electrode geometry and the magnitude of electric potential on the velocity of these flows.

2. Materials and experimental method

2.1. Materials

Particle-covered droplets comprised silicone oil (VWR Chemicals, Rhodorsil 6678.1000, viscosity ~50 mPa·s, density ~0.96 g·cm^{-3}, relative permittivity ~2.8, and electrical conductivity ~5 pS·m^{-1}) and PE particles (Cospheric LLC, REDPMS-0.98/BLPMS-0.98, size 45–53 μm, density ~0.98 g·cm^{-3}, relative permittivity ~2.1 and electrical conductivity ~10^{-15} S·m^{-1}). First, we dispersed the PE particles in silicone oil. Then using a mechanical pipette, we formed a dispersion droplet inside castor oil (Sigma-Aldrich 83912, viscosity ~750 mPa·s, density ~0.96 g·cm^{-3}, relative permittivity ~4.7, and electrical conductivity ~100 pS·m^{-1}). In this scenario, most of the PE particles resided inside the droplet. To bring the particles to the silicone oil–castor oil interface, we used an *E*-field, as described in ref. [47]. Once the particles reached the interface, they strongly bound to it with a binding energy of ~10^4 k_BT.

2.2. Experimental method

The experimental setup comprised a signal generator (SDG1025, SIGLENT), a high-voltage bipolar amplifier (10HVA24-BP1, HVP High Voltage Products GmbH), a digital microscope (AM7115MZTL, Dino-Lite Digital Microscope) for observation at an angle (~20°) perpendicular to the direction of the applied *E*-field, a light source, a PC for recording movies, and an acrylic cuvette (15 mm × 15 mm × 30 mm) used as a sample cell. The sample cell was placed on a mechanical XYZ-translation stage (LT3, Thorlabs, Sweden) for simple positioning relative to the optical path of the microscope. The bottom wall of the cell was made of a glass-coated indium tin oxide thin layer, which served as an electrode. The signal electrode was placed above a particle-covered droplet (inserted from the open top of the sample cell and immersed in castor oil). For the signal electrode, we used materials with different shapes: a stainless-steel cylindrical electrode (diameter of 0.1–3 mm) and a copper plate electrode. A high-voltage bipolar signal was provided to the sample cell via two crocodile clips attached to the top and bottom electrodes. The distance between the electrodes (h) was adjusted according to the requirements of the experiment. A stainless-steel O-ring was attached to the conductive bottom of the sample cell (at its center) to hold the droplet in place and to prevent its electrorotation—a phenomenon that occurs under strong *E*-fields [48].

2.3. PIV experiment

The EHD flows induced around a particle-covered droplet and near the tip of a nonplanar electrode were traced *via* PIV. Blue PE particles (Cospheric LLC, BLPPMS-1.00, size ~30 μm, and density ~1.00 g·cm^{-3}) used as tracer particles were dispersed in castor oil and poured into the sample cell. A silicone oil droplet (~4 mm) coated with 50-μm PE particles was suspended in the dispersion medium and docked into the conductive O-ring. An electric potential of varying intensity (1.3–2.6 kV) was provided to the signal electrode, which resulted in the generation of liquid flows in the system. We recorded movies at a speed of 10 fps and a resolution of 1280 × 960 pixels using a digital microscope (AM7115MZTL, DINO-LITE). From each movie, 150 sequential frames were extracted and used to generate flow field maps using MATLAB® software (v.R2017b, MathWorks®) and its PIV Toolbox™.

2.4. Droplet deformation

The Taylor–Melcher leaky dielectric model [49] describes *E*-field-driven hydrodynamic phenomena in weakly conducting liquids: liquids that are described as dielectric materials having small Ohmic conductivities. The model can be used to estimate the magnitude of deformation of poorly conducting droplets suspended in another poorly conducting medium under an applied *E*-field. The model is based on the assumption that the free charges accumulate at the droplet interface, generating the compressive electric stress, thereby deforming the droplet. The magnitude of droplet deformation depends on both the relationship between surface tension (γ) and normal electric stress and the stability between viscous stresses (associated with hydrodynamic currents in the droplet and its surroundings) and the tangential electric stress, which is given as follows:

$$D = \left(\frac{d_{\parallel} - d_{\perp}}{d_{\parallel} + d_{\perp}}\right) = \frac{9 r_0 \varepsilon_0 \varepsilon_{ex} E_0^2}{16 \gamma S (2+R)^2}\left[S\left(R^2+1\right) - 2 + 3(RS-1)\frac{2\lambda+3}{5\lambda+5}\right] \quad (1)$$

where $d_{\parallel}$ and $d_{\perp}$ are the droplet axes parallel and perpendicular to the direction of the applied *E*-field, respectively; ε_0 is the vacuum permittivity; ε_{ex} is the permittivity of the surrounding liquid; r_0 is the radius of the droplet; and the dimensionless numbers *R*, *S*, and λ represent the conductivity, dielectric constant, and viscosity ratios, which are defined as: $R = \frac{\sigma_{in}}{\sigma_{ex}}$, $S = \frac{\epsilon_{ex}}{\epsilon_{in}}$, and $\lambda = \frac{\mu_{ex}}{\mu_{in}}$, respectively. This model is applicable only for small deformations and for a droplet placed in a uniform *E*-field. However, we will use it in this study for a coarse estimation of the droplet deformation.

2.5. Modeling of the E-field distribution using the finite element method

The configuration of the cylindrical–plate electrode under consideration is shown in Fig. 1**(a)**. A cylindrical electrode of diameter *d* is placed perpendicular to the plate electrode at distance *h*. The diameter *d* and the gap between the electrodes *h* (filled with castor oil) are the parameters that define the geometry and determine the *E*-field strength. The *E*-field or potential distribution may only change along the radial direction, perpendicular to the plate electrode along the gap. Therefore, the task may be reduced into a two-dimensional axisymmetric problem. For modeling of the *E*-field distribution, we used the COMSOL Multiphysics v.5.5 software package. A surface plot of the *E*-field strength distribution across the electrode gap is shown in Fig. 1**(b)**. An example of the

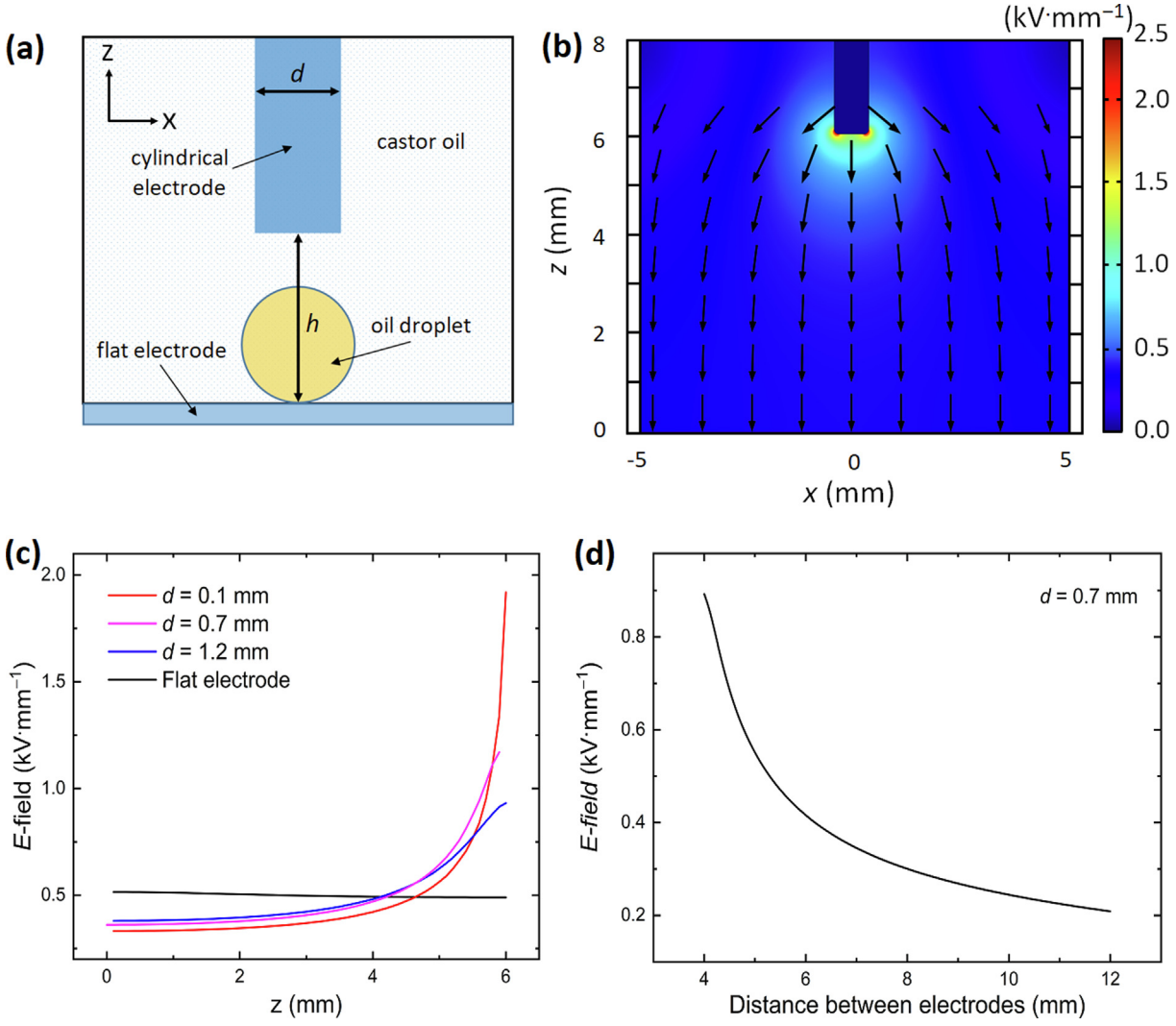

Fig. 1. **(a)** Configuration of the cylindrical–plate electrode system with a particle-covered droplet placed at the bottom of the container. **(b)** *E*-field intensity map at U = 3 kV, h = 6 mm, and d = 0.7 mm. **(c)** *E*-field intensity across the gap (*z*-axis) at U = 3 kV and h = 6 mm for different top-electrode geometries. **(d)** *E*-field intensity between the different electrode gaps at U = 3 kV and d = 0.7 mm. U is estimated by averaging the modeled *E*-field values along the upper hemisphere of the droplet interface.

calculated variation in the *E*-field intensity across the gap (*z*-axis) is shown in Fig. 1**(c)**. The calculations were performed for four top-electrode geometries kept at a fixed distance h = 6 mm under an electric potential of 3 kV. Furthermore, we calculated the *E*-field strength at the coordinates $x = 0$ and $z = 4$ mm (i.e., at the position of the 4-mm droplet's top surface) for different electrode-gap values [Fig. 1**(d)**]. An electric potential of 3 kV was applied between the cylindrical electrode (d = 0.7 mm) and plate electrode. The *E*-field acting on the droplet was calculated by averaging the *z*-components of the *E*-field strength over the upper hemisphere of the droplet interface. The *E*-field strengths for different electrode configurations and electric potentials were treated as the input values for the Melcher–Taylor equation [**Eq. (1)**].

3. Results and discussion

3.1. Effect of electrode geometry on droplet deformation

The deformation of a particle-covered silicone oil droplet under a uniform *E*-field was studied in previous works [26,27,50]. In this study, we investigate the effect of different electrode geometries on the droplet deformation under both uniform and nonuniform *E*-fields. We prepared a silicone oil droplet (~4.4 mm) covered with 50-μm PE particles that was suspended in castor oil and docked (sedimented) into the stainless-steel O-ring attached to the conductive bottom of the sample cell. A signal electrode was placed at a fixed electrode distance (~8 mm), and the electric potential was increased in a stepwise manner. At each step, the electric potential was increased by ~0.13 kV, and steady-state of droplet deformation and particle rearrangement were achieved in 1 min. Four sizes of top electrodes were used: a plate electrode and three cylindrical electrodes (with diameters of 0.1, 1.2, and 3.0 mm). The electrodes are shown in the inset in Fig. 2**(a)**, in which a droplet is subjected to an electric potential of ~2.2 kV.

In Fig. 2, the magnitude of droplet deformation is plotted as a function of electric potential. The experimental results [Fig. 2**(a)**] demonstrated that the deformation magnitude was consistently higher for a uniform *E*-field compared to that of a nonuniform *E*-field. The data showed that under a nonuniform *E*-field, the deformation magnitude decreased with the decrease in electrode diameter and deforms the least under the electrode of the smallest diameter (~0.1 mm). This could be because of the differences in the *E*-field distribution for the different electrode geometries.

We modeled the *E*-field distribution using the finite element method to estimate the magnitude of the droplet deformation using the Melcher–Taylor equation [**Eq. (1)**] and then compare the calculated values with the experimental data.

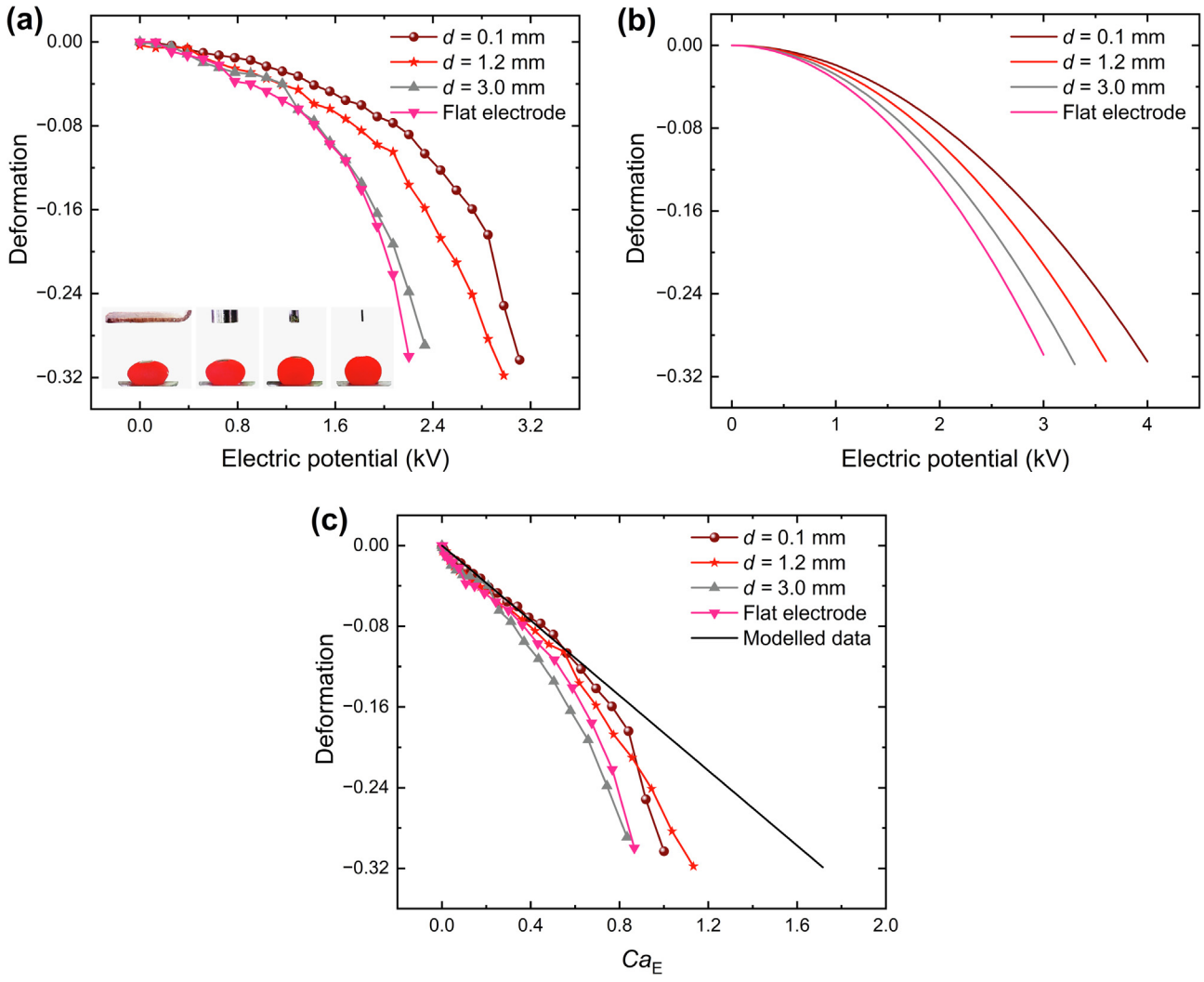

Fig. 2. Effect of electrode geometry on the magnitude of droplet deformation. Four sizes of top electrodes were used (see inset images), which were placed at a fixed distance of 8 mm. **(a)** Experiential and **(b)** modeled data of the magnitude of droplet deformation as a function of the applied electric potential. **(c)** Droplet deformation is plotted as a function of the electric capillary number, $Ca_E = \frac{r_0 \varepsilon_0 \varepsilon_{ex} E_0^2}{\gamma}$.

In Fig. 2**(b)**, we plot the calculated values of the magnitude of droplet deformation for different electrode geometries as a function of applied electric potential. The results obtained from the model show good qualitative agreement with the experimental results but quantitatively the magnitude of droplet deformation is smaller. The main reason for this is that the formula for droplet deformation described in **Eq. (1)** is valid for small deformations, namely, below approximately −0.1. In Fig. 2**(c),** the values of experimentally measured droplet deformations are plotted as a function of the electric capillary number $Ca_E = \frac{r_0 \varepsilon_0 \varepsilon_{ex} E_0^2}{\gamma}$, where γ is the interfacial tension. We included the modeled data. The results showed that at a lower electric capillary number (maximum $Ca_E \approx 0.3$), the deformation of the droplet for each electrode follows the modeled data. For a larger electric capillary number ($Ca_E > 0.3$), the droplet deformations begin to considerably deviate.

As shown in Fig. 2**(a)**, the maximum value of the measured deformation is approximately −0.33. Therefore, at deformations of $D > -0.35$, the droplet shape becomes asymmetrical and at very strong *E*-fields, the particle shell becomes unstable and droplet breakup may occur.

After understanding the effect of electrode geometry on droplet deformation at a fixed electrode distance, we decided to further study the deformation by minimizing the gap between the electrodes to the point where the electrodes touched the droplet. As shown in Fig. 3, we experimentally and theoretically estimated the magnitude of droplet deformation. The droplet was subjected to a fixed DC electric potential of ∼0.8 kV using two top-electrode shapes: (i) a cylindrical electrode (diameter 0.7 mm) and (ii) a plate electrode. At such a low electric potential, the droplet touched the top electrodes without affecting the particle shell. Initially, the cylindrical electrode was placed above the droplet at a distance of ∼12 mm from the bottom electrode. The strength of the *E*-field was increased stepwise by lowering (∼0.25 mm) the top electrode. We found that at electrode distances of ∼6 mm or more, the magnitude of droplet deformation using the cylindrical electrode increased more slowly (ΔD ∼0.03) compared to that of the plate electrode (ΔD ∼0.07) [Fig. 3**(a)**]. Upon further decreasing of the distance between the electrodes (below ∼6 mm), the magnitude of droplet deformation using the cylindrical electrode started to increase steeply but the deformation magnitude was still smaller than that of the plate electrode. However, when the top electrode nearly touched the droplet (below an electrode distance of ∼4 mm), the droplet deformed strongly using the cylindrical electrode and crossed the magnitude of the deformation curve using the plate electrode. The modeled result showed a similar crossing point for the magnitude of the droplet deformation curve when the electrodes touched the droplet [Fig. 3**(b)**]. The charge density on the surface of an electrode depends on its shape, such that an increased curvature affords a higher free-charge density. This affords the generation of a locally strong *E*-field [39]. Thus, the *E*-field intensity at the tip of a cylindrical electrode is much stronger than that generated below a plate electrode.

3.2. Electric potential-induced deformation of the particle shell

In this experiment, we prepared a silicone droplet (∼4.3 mm) covered by PE particles placed in castor oil. The droplet was subjected to a nonuniform *E*-field by applying a constant DC electric

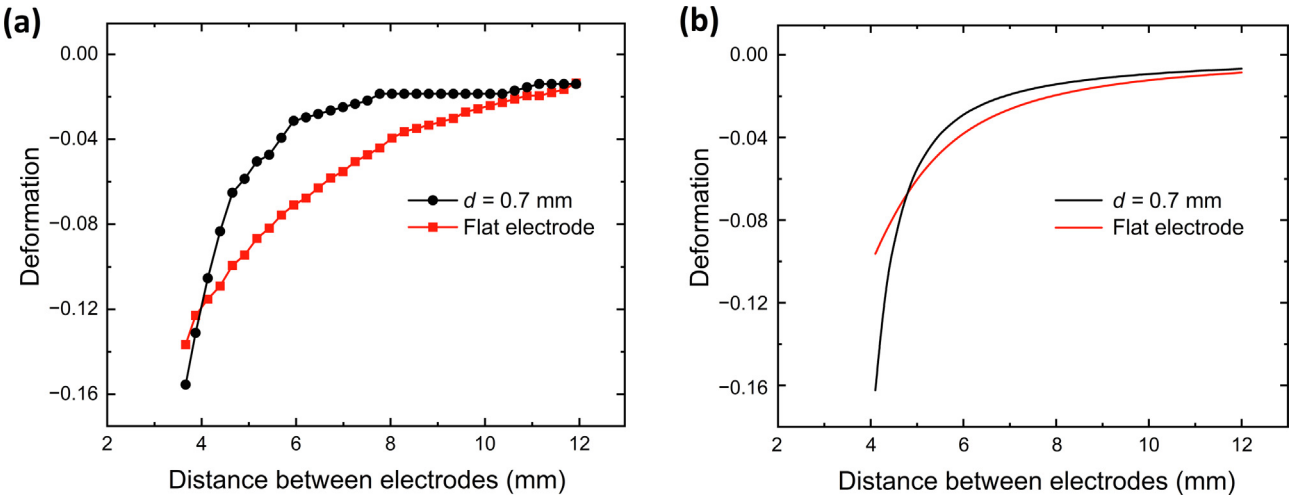

Fig. 3. Deformation of silicone oil droplet (∼4.3 mm) covered with 50-μm PE particles plotted as a function of the distance between electrodes (h). A stainless-steel cylindrical electrode with a diameter of ∼0.7 mm and a plate electrode used as a top electrode were at a fixed DC potential of ∼0.8 kV. The *E*-field strength was increased stepwise by minimizing the distance between the electrodes. The magnitude of droplet deformation was thus estimated **(a)** experimentally and **(b)** theoretically.

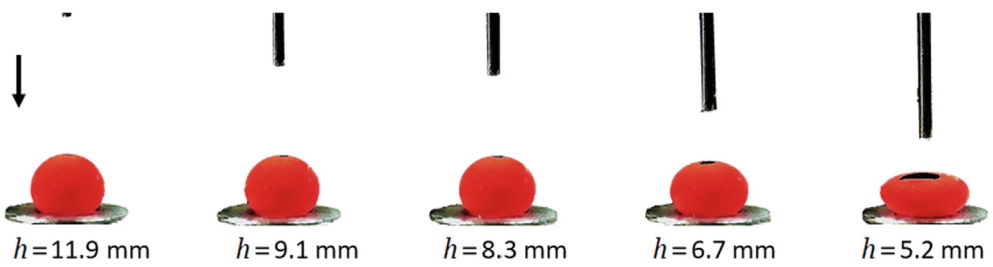

Fig. 4. Silicone oil droplet (size ∼4.3 mm) covered with PE particles placed inside castor oil and attached to the conductive bottom of the sample cell through a stainless-steel O-ring. A cylindrical electrode (diameter ∼0.7 mm) was used as a top electrode and connected to an electric potential of ∼2 kV. The strength of the *E*-field was increased by lowering the top electrode.

potential of ~0.6–3.9 kV. Initially, the cylindrical electrode (diameter ~0.7 mm) was placed at a distance of ~12 mm from the bottom electrode. The strength of the *E*-field was increased stepwise by lowering the top electrode in a manner similar to the previous experiment. Under a constant electric potential, with each step of minimizing the electrode distance, the magnitude of droplet deformation and the opening area at the electric pole increased (Fig. 4**)**.

In Fig. 5**(a)**, the magnitude of droplet deformation is plotted as a function of the distance between the electrodes. We theoretically estimated the magnitude of droplet deformation at different electric potentials by inserting the values of *E*-field strength (measured at the interface of a 4-mm droplet, i.e., at the coordinates $x = 0$ and $z = 4$ mm) in **Eq. (1)**, as obtained using COMSOL simulations [Fig. 5 **(b)**]. The results show good qualitative agreement with the experimental data for small deformations. However, under stronger *E*-fields, the experimentally observed deformations were bigger than those predicted by the Melcher–Taylor model [49], and this discrepancy increased with increasing *E*-field strength [compare Fig. 5**(a)** and Fig. 5**(b)**].

The rate of change of deformation clearly depends on the value of the applied electric potential. To find the rate of change of *D* (within the studied range of h = 4–12 mm), we use an empirical model of the form $D = -A/h^n$, where A and n are the fit coefficients. Fig. 5**(c)** shows the dependence of the scale index n, which is the measure of the rate of change of *D*, on the electric potential. Upon increasing the electric potential, n increases (so as the discrepancies between the observed deformations and those predicted by Taylor's model). As the electric potential is reduced to zero, the value of $n \to 2$. Thus, if the electrode is brought within close proximity to the droplet surface and a low electric potential is applied, the magnitude of *D* does not considerably change (and can be better tuned) when the electrode is translated vertically over a small distance. This could be beneficial, for example, for opening a particle shell and manipulating the droplet liquid, as shown in Section 3.3.

3.3. Formation of an opening in a particle shell

When a droplet deforms, its surface area increases. In the case of the particle-covered droplet studied herein, the increased surface area causes the unjamming of particles in the shell and the formation of a particle-free area. A circular opening in the particle layer is created via the induced EHD flows that convect particles away from the droplet's electric pole (for more details, see ref. [40]). In this section, we study the relationship between the applied *E*-field as well as the size opening and investigate the limits of the electric potential that can be used to form an opening without affecting the shell or breaking up the droplet. Moreover, we illustrate examples of the practical application of the particle shell opening.

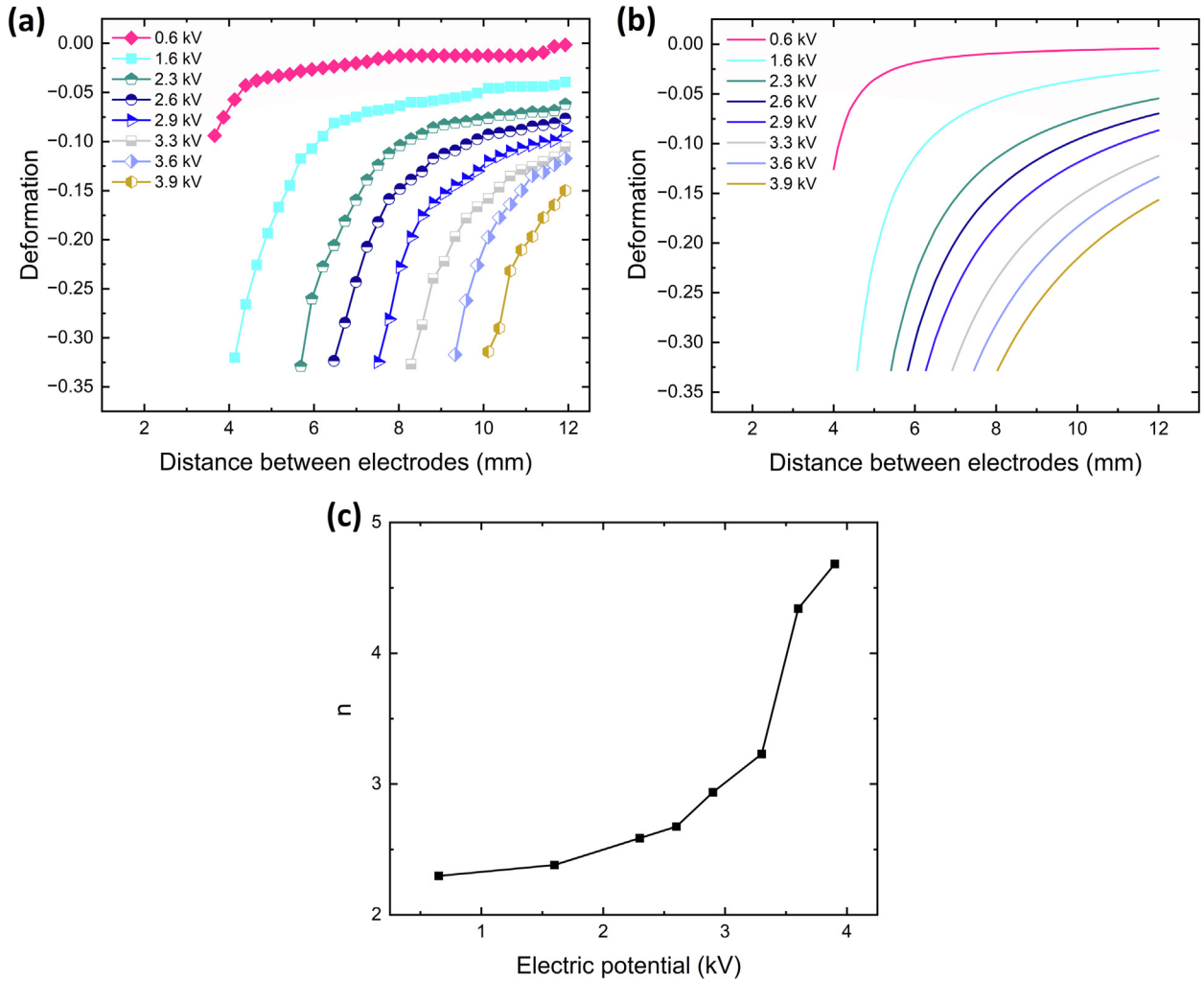

Fig. 5. **(a)** Deformation of silicone oil droplet (~4.3 mm) covered with PE particles plotted as a function of electrode distance. **(b)** The magnitude of *D* is calculated theoretically at different electric potentials (0.6–3.9 kV). **(c)** The dependence of the scale index on the applied electric potential.

In Fig. 6**(a)**, we plotted the opening area A (normalized by $S_0 + A$, where $S_0 = 4\pi r_0^2$ is the surface area of the droplet) as a function of electrode distance obtained experimentally, as shown in Fig. 4 and Fig. 5 (i.e., droplet size ~4.3 mm; electrode with diameter ~0.7 mm). At lower electric potentials (e.g., 130 and 250 V), no opening area was observed at the droplet electrical pole until the gap between the electrodes were ~4.9 mm and ~6.7 mm. This is because the droplet was hardly deformed, and the particles formed a jammed monolayer at the droplet surface. However, at a stronger electric potential (above ~250 V), the droplet started deforming more and the magnitude of deformation increased upon lowering the top electrode. Thus, the total area of the droplet increased, allowing the particle layer to unjam. The EHD flows generated at the fluid–fluid interface directed from the droplet poles to the droplet equator created an opening area at the droplet's electric pole, which became wider at higher deformation magnitudes.

The size of the opening area at the droplet's pole should be proportional to the change in the total area of the droplet after deformation, assuming that the particle packing of the particles forming the shell is not altered. In Fig. 6**(b)**, we plotted the normalized opening area at the droplet pole as a function of the absolute value of the droplet deformation under different electric potentials (1.6–3.9 kV). We found that the data at the different electric potentials were overlapping. Under the same applied electric stress, the opening area at the droplet pole depends on the change in the total sur-

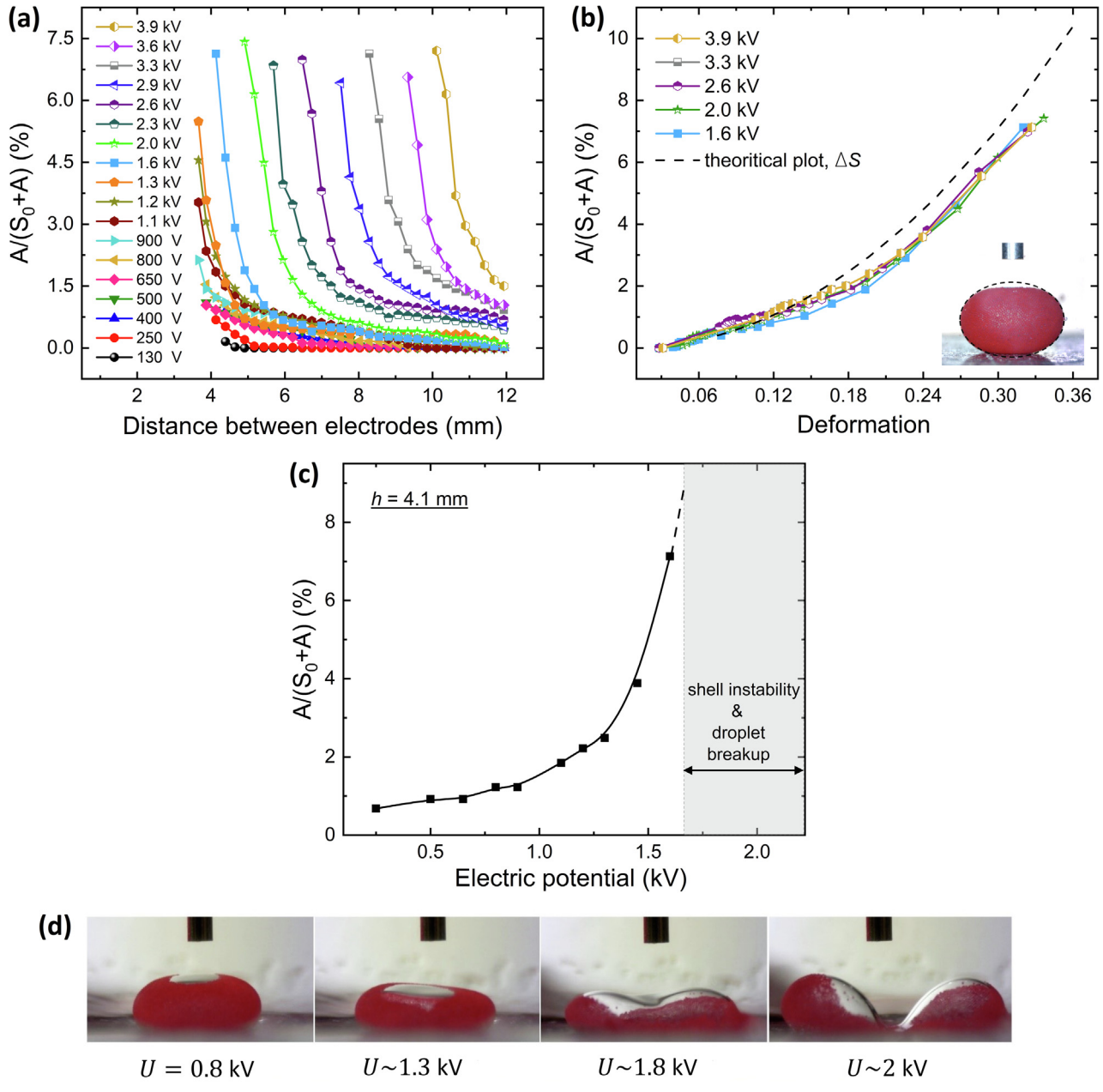

Fig. 6. **(a)** Normalized opening area of the particle layer plotted as **(a)** a function of the distance between electrodes and **(b)** as a function of the absolute value of droplet deformation. The dashed curve represents the model values of the change in surface area (ΔS) of an oblate spheroid with a volume corresponding to that of the droplet used in the experiment. **(c)** Normalized opening area of the particle shell *vs*. electric potential for electrodes kept at h = 4.1 mm. A strong electric potential (gray area) was applied, resulting in shell instability or droplet breakup. **(d)** A 1.8-mm silicone oil droplet covered by 50-μm PE particles subjected to different DC electric potential strengths through the top electrode, with a diameter of ~0.5 mm and an electrode gap of ~2.2 mm. A steady-state is achievable when U is below approximately 1.2 kV. Application of a greater electric potential yields particle-shell instability (particles circulate), particle detachment from the interface, and possibly droplet breakup.

face area of the droplet and that the particle packing in the shell remains similar.

In Fig. 6**(b)**, we plot theoretically calculated values of the change in surface area (ΔS) of the oblate spheroid. The experimental values were lower than the modeled values for larger deformations (i.e., $D > 0.15$). This is because the deformed droplet is not an ideal oblate spheroid, i.e., it flattens at the droplet's electric poles [see the inset of the image in Fig. 6**(b)**] and may even form a dimple when a strong electric potential is provided to the cylindrical electrode.

In Fig. 6**(c)**, we plot the values of the normalized opening area of the particle shell against the electric potential. Because the signal electrode was maintained at h = 4.1 mm, nearly in contact with the droplet, the maximum electric potential was 1.6 kV. Stronger electric potentials afforded the asymmetric deformation of the droplet and the instability of the particle shell, and at very high E-fields, the droplet may break up [see also Fig. 6**(d)**].

That data presented in Fig. 6**(c)** can be useful, for example, for designing a procedure for manipulating a droplet liquid. In Fig. 7 **(a)**, we demonstrate that the electric method enables the insertion of a material into a droplet without affecting the particle shell. For this, we used a needle with an outer diameter of ~0.8 mm that had a dual function: an electrode, allowing the formation of an opening in the particle shell and as a conduit for conveying (adding or removing) material to and from the droplet. In the experiment, the needle was at a fixed potential of approximately 800 V. At this moderate electric potential, a sufficiently large opening was created to insert the needle into the droplet without touching the particles. Then, we injected a small amount of silicone oil with a 250-μm PE particle (red particle in the middle panel) and allowed the sedimentation of particles. Next, the electrode was lifted and a small volume of oil (similar to that injected into the droplet) was sucked out. After that, we turned off the electric potential. It took several seconds for the particle shell to close. It is interesting to note, that a stable dimple-shaped deformation could be obtained using a cylindrical electrode with a diameter smaller than the diameter of the droplet [Fig. 7**(a)**]. Such a shape could not be obtained when using plate electrodes.

In another experiment, we demonstrated that method to deform a droplet under an E-field can be used for inspecting the interior content of a particle-covered droplet. In Fig. 7**(b)**, a particle-covered droplet with inserted 250-μm PE particles is viewed from above. The camera view was approximately 10°-away from the vertical axis. The electrode was placed far away from the droplet (h ~15 mm) to enable a clear camera view. After an electric potential of 2.6 kV was applied to the electrode, the surface particles moved away from the droplet's electric pole and formed an opening in the particle shell. This allowed us to inspect the presence of the particles inside the droplet.

3.4. PIV analysis with different electrode geometries

In this section, we study the effect of electrode geometry and different applied electric potentials on the magnitude and direction of the E-field-induced liquid flows in the sample cell by performing PIV experiments.

As seen in Fig. 8**(a–c),** a particle-covered droplet was subjected to an electric potential of 2 kV with three top-electrode geometries. The results of the PIV experiments showed that the induced liquid flows were greatly influenced by the geometry of the electrodes.

In the case of the plate–plate electrode configuration, the magnitude of the EHD flows was the greatest next to the droplet's surface (~100 $\mu m \cdot s^{-1}$). When the top electrode was changed from plate to cylindrical electrode, the flow velocity just below the top electrode was increased from nearly 0 to ~500 $\mu m \cdot s^{-1}$. In addition, the convective motion of liquids had a different pattern—a jet shape. In Fig. 8**(g)**, we plot the variation in EHD flows velocity across the electrode gap (along the vertical axis of image symmetry), which corresponds to the PIV maps presented in panels (a, c). The peaks in the plot are in different places, and their values differ. The induced liquid flows have different physical origins. In the plate–plate electrode configuration (uniform E-field), the EHD flows originate from the jump in the tangential component of the electric stress [42–44]. By contrast, for the cylindrical–plate electrode configuration, the flows are likely induced through ion injection at the metal–liquid interface [46,51]. Similar flow patterns are observed in the presence and absence of the droplet, which confirms that the flows are induced by a different mechanism than that described by Taylor.

As seen in Fig. 8**(d–f)**, we kept the electrode distance fixed, and the droplet was subjected to different DC electric potentials (1.3–2.6 kV). For the lowest electric potential (1.3 kV), the EHD flows were strong near the tip of the electrode and the flow velocity was ~200 $\mu m \cdot s^{-1}$. When the potential was increased to 2.6 kV the flow velocity increased to ~550 $\mu m \cdot s^{-1}$ and the area where the velocity of the flows was the highest had shifted farther away from the electrode. In Fig. 8**(h)**, we plot the variation in EHD flow velocity across the gap, which corresponds to the PIV maps pre-

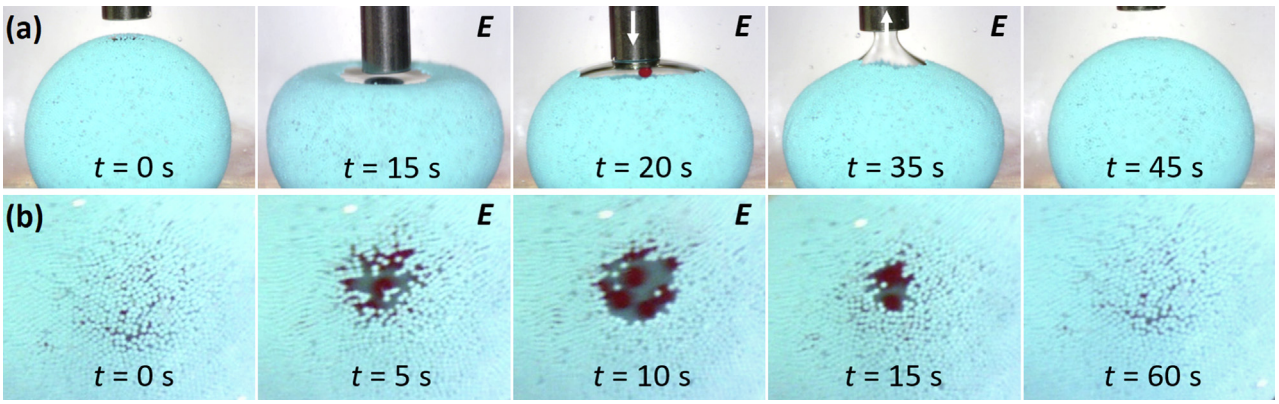

Fig. 7. (a) Injecting a 250-μm PE particle into a particle-armored silicone oil droplet (~3.4 mm). After an electric potential of 800 V was applied to the cylindrical electrode (~0.8 mm), an opening at the particle shell was formed and grew in size as the electrode was brought closer to the droplet. This allowed for injecting a small amount of particle dispersion (see middle panel). After the injection, a small amount of silicone oil was sucked out and then the electric potential was turned off, enabling the droplet to relax and the particle shell to recover. **(b)** Inspecting the interior content of the particle-covered droplet. An electric potential of 2.6 kV was applied to the electrode kept at a fixed distance of ~15 mm. The surface particles moved away from the droplet's electric pole and formed an opening area, which allowed for the inspection of materials inside the droplet.

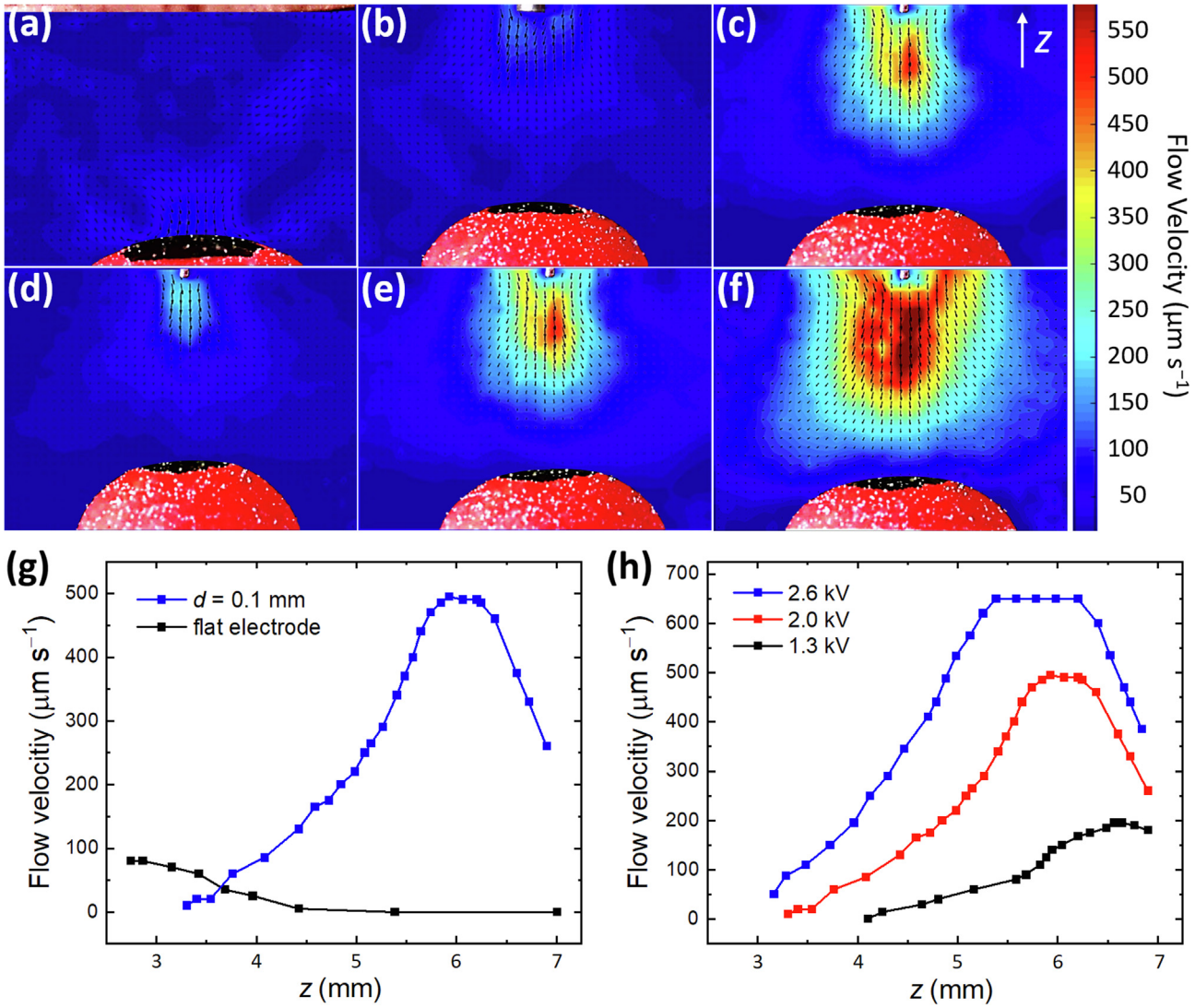

Fig. 8. PIV images of a silicone oil droplet (~4 mm) covered with PE particles and placed at the conductive bottom of the sample cell. **(a–c)** The droplet was subjected to a fixed electric potential of 2.0 kV applied through different electrode geometries, i.e., a plate electrode and cylindrical electrodes (diameter ~0.1 mm and diameter ~0.6 mm), at a fixed electrode distance of ~7 mm. **(d–f)** The droplet was subjected to different strengths of DC electric potential: 1.3 kV, 2.0 kV, and 2.6 kV, respectively, at a fixed electrode distance of 7 mm. **(g,h)** The variation in EHD flow velocity across the gap, which corresponds to (a–c) and (d–f), respectively.

sented in panels (d–f). The magnitude of the induced flows increases with the increase in the applied electric potential, and the peaks move farther away from the electrode. Similar observations were made by Traore et al. [46] and Perri et al. [52], who analyzed liquid flows using numerical simulation and PIV experiments.

4. Discussion and conclusions

In this study, we used non-uniform DC *E*-fields to induce compressive electric stress on a Pickering droplet. The deformation of the droplet was examined as a function of the applied electric potential, the distance between the electrodes, and the shape of the signal electrode (as well as the droplet's size, see **Fig. S1**). Our experimental results were compared with modeled calculations. The results show good qualitative agreement with the experimental data. There is some discrepancy observed in the magnitude of the droplet deformation (particularly for large deformations). The main reason for this is that the formula for droplet's deformation described in **Eq. (1)** is only valid for small deformations. At larger deformations, the droplet's surface area (ΔS) increases sharply [see Fig. 6(**b**)], allowing a larger number of charges to accumulate at the liquid–liquid interface. This, in turn, creates stronger electric stresses, which may increasingly deform the droplet (if overcoming the opposite force stemming from the surface tension and the Laplace pressure). We should highlight that we modeled the *E*-field distribution between the electrodes without including the droplet. We assumed that the droplet's presence does not considerably affect the field distribution because the electrical and dielectric properties of both the particles forming a shell and the silicone oil droplet are comparable with those of the surrounding liquid. Still, the omission of the particle-covered droplet may yield the data discrepancy.

The shape of the droplet deformed by a cylindrical electrode (with the diameter smaller than the size of the droplet) placed near the droplet's surface may differ from the shape of a droplet deformed by a uniform field using plate–plate electrodes. The droplet's shape considerably deviates from the shape of an oblate spheroid, i.e., it flattens at the droplet's electric poles [see the inset of the image in Fig. 6(**b**)], and may even dimple when a strong *E*-field is generated [see Fig. 7(**a**)]. The dimpling of droplets was observed by other researchers that used uniform [53,54] and nonuniform [55,56] *E*-fields. Herein, a stable dimple-shape droplet

could be formed [see Fig. 7**(a)**] when a non-uniform *E*-field is created by placing a thin electrode near to the surface. We think it would be interesting to study this more closely both experimentally and theoretically.

We also studied the structuring of particles at the droplet interface that caused formation of an opening area. We showed that the size of the opening area can be controlled by changing the electrode distance and the applied electric potential. We then demonstrated that this allowed for designing procedures for the injection of a material into a droplet and the inspection of the interior content of the particle-covered droplet without affecting its particle shell. This approach involving *E*-field could be used to facilitate chemical reactions in droplets and enable various small-scale laboratory operations, creating new possibilities for applications in clinical diagnostics, microfluidics, and material engineering.

We also studied the effects of different electrode geometries and applied *E*-fields on the magnitude and direction of the EHD flows using the PIV method. We found that the circulation of liquid in a sample cell originates from two mechanisms. In the plate–plate electrode configuration (uniform *E*-field), the EHD flows originate from the jump in the tangential component of the electric stress, i.e., circulating flows are formed to compensate for the difference in tangential stress caused by the hydrodynamic stress. For the cylindrical–plate electrode configuration, the flows are induced through chemical reaction at the surface of the cylindrical electrode, which causes the ion injection and a local accumulation of charges. To study the influence of such ion injection in greater detail would be interesting, for example, on the transient deformation of a droplet and heat-transfer enhancement [57–60].

The findings of our studies can be important for applications in electrocoalescence as well as electroemulsification. Moreover, they are important for designing electrodes for droplet-based microfluidic systems. We expect that our work will influence further studies on the effect of a non-uniform *E*-field on the deformation of particle-covered droplets.

Declaration of Competing Interest

The authors declare that they have no known competing financial interests or personal relationships that could have appeared to influence the work reported in this paper.

Acknowledgements

This research was funded by the Polish National Science Centre through PRELUDIUM (2019/35/N/ST5/02821) and OPUS (2015/19/B/ST3/03055) programs and by the European Social Fund under the project: UNIVERSITY OF TOMORROW - integrated development program for the University of Adam Mickiewicz in Poznań (POWR 03.05.00-00-Z303/17). We also thank the Research Council of Norway for its support through the Centres of Excellence funding scheme (project no. 262644).

Author Contributions

K. K. initiated the project and designed and performed all of the experiments. T. H. modeled for the calculations. K. K. authored the first draft of the manuscript. K. K., T. H., and Z. R. took part in discussions toward the finalization of the manuscript. All authors have read and agreed to the final version of the manuscript.

Appendix A. Supplementary material

Supplementary data to this article can be found online at https://doi.org/10.1016/j.molliq.2022.118834.

References

[1] A. Fery, R. Weinkamer, Polymer 48 (2007) 7221.
[2] C.L. Tucker Iii, P. Moldenaers, Annu. Rev. Fluid Mech. 34 (2002) 177.
[3] Y. Zhu, H. Gao, W. Liu, L. Zou, D.J. McClements, J. Texture Stud. 51 (2020) 45.
[4] S. Wang, Y. Zhong, H. Fang, J. Fluid Mech. 869 (2019) 634.
[5] Y. Chang, X. Chen, Y. Zhou, J. Wan, Ind. Eng. Chem. Res. 59 (2020) 3916.
[6] F. Mostowfi, K. Khristov, J. Czarnecki, J. Masliyah, S. Bhattacharjee, Appl. Phys. Lett. 90 (2007) 184102.
[7] Y. Peng, T. Liu, H. Gong, X. Zhang, Int. J. Chem. Eng. 2016 (2016) 2492453.
[8] F. Fanalista et al., ACS Nano 13 (2019) 5439.
[9] P. Lele, A.H. Syed, J. Riordon, N. Mosavat, A. Guerrero, H. Fadaei, D. Sinton, J. Pet. Sci. Eng. 165 (2018) 298.
[10] C.C. Berton-Carabin, K. Schroën, Annu. Rev. Food Sci. Technol. 6 (2015) 263.
[11] C. Albert, M. Beladjine, N. Tsapis, E. Fattal, F. Agnely, N. Huang, J. Control. Release 309 (2019) 302.
[12] D. Terescenco, N. Hucher, C. Picard, G. Savary, Int. J. Cosmet. Sci. 42 (2020) 198.
[13] A. Heyse, C. Plikat, M. Grün, S. Delaval, M. Ansorge-Schumacher, A. Drews, Process Biochem. 72 (2018) 86.
[14] P. He, Y. Liu, R. Qiao, Microfluidics and Nanofluidics 18 (2015) 569.
[15] Y. Jiang, X. Liu, Y. Chen, L. Zhou, Y. He, L. Ma, J. Gao, Bioresour Technol 153 (2014) 278.
[16] Y. Chevalier, M.-A. Bolzinger, and S. Briançon, 267–281, Springer-Verlag Berlin Heidelberg (2015).
[17] S.M. Dieng, N. Anton, P. Bouriat, O. Thioune, P.M. Sy, N. Massaddeq, S. Enharrar, M. Diarra, T. Vandamme, Soft Matter 15 (2019) 8164.
[18] F. Sicard, J. Toro-Mendoza, ACS Nano (2021).
[19] M.P. Neubauer, M. Poehlmann, A. Fery, Adv. Colloid Interface Sci. 207 (2014) 65.
[20] A.B. Subramaniam, M. Abkarian, L. Mahadevan, H.A. Stone, Langmuir 22 (2006) 10204.
[21] S.Y. Tan, R.F. Tabor, L. Ong, G.W. Stevens, R.R. Dagastine, Soft Matter 8 (2012) 3112.
[22] R. Finken, S. Kessler, U. Seifert, J. Condens, Matter Phys. 23 (2011) 184113.
[23] H.H. Boltz, J. Kierfeld, Phys. Rev. E 92 (2015) 033003.
[24] C. Wischnewski, J. Kierfeld, Phys. Rev. Fluids 3 (2018) 043603.
[25] A. Mikkelsen, Z. Rozynek, A.C.S. Appl, Mater. Interfaces 11 (2019) 29396.
[26] A. Mikkelsen, P. Dommersnes, Z. Rozynek, A. Gholamipour-Shirazi, M.D.S. Carvalho, J.O. Fossum, Materials 10 (2017) 436.
[27] A. Mikkelsen, K. Khobaib, F.K. Eriksen, K.J. Måløy, Z. Rozynek, Soft Matter 14 (2018) 5442.
[28] Z. Rozynek, J. Banaszak, A. Mikkelsen, K. Khobaib, A. Magdziarz, Soft Matter (2021).
[29] Z. Rozynek, K. Khobaib, A. Mikkelsen, A.C.S. Appl, Mater. Interfaces 11 (2019) 22840.
[30] P.F. Salipante, P.M. Vlahovska, Phys. Fluids 22 (2010) 112110.
[31] R.B. Karyappa, S.D. Deshmukh, R.M. Thaokar, Phys. Fluids 26 (2014) 122108.
[32] N. Bentenitis, S. Krause, Langmuir 21 (2005) 6194.
[33] D. Das, D. Saintillan, J. Fluid Mech. 829 (2017) 127.
[34] Y. Yao, Y. Wang, K.M. Beussman, Microfluidics Nanofluidics 17 (2014) 907.
[35] C. Song, Q. Chen, X. Wang, L. Wen, T. Zheng, IEEE 11th Intern, Confer. (ICPADM) 652 (2015).
[36] S. Mhatre, R.M. Thaokar, Phys. Fluids 25 (2013) 072105.
[37] J.Q. Feng, Phys. Rev. E 54 (1996) 4438.
[38] S.D. Deshmukh, R.M. Thaokar, J. Fluid Mech. 731 (2013) 713.
[39] M.M. Ahn, D.J. Im, I.S. Kang, Analyst 138 (2013) 7362.
[40] K. Khobaib, T. Hornowski, Z. Rozynek, Phys. Rev. E 103 (2021) 062605.
[41] Y. Zhao, J. Fang, H. Wang, X. Wang, T. Lin, Adv. Mater. 22 (2010) 707.
[42] G. Taylor, Proc. R. Soc. Lond. A 291 (1966) 159.
[43] J.Q. Feng, Proc. R. Soc. A 455 (1999) 2245.
[44] A. Esmaeeli, P. Sharifi, Phys. Rev. E 84 (2011) 036308.
[45] D.J. Im, I.S. Kang, J. Colloid Interface Sci. 266 (2003) 127.
[46] P. Traore, M. Daaboul, C. Louste, J. Phys. D 43 (2010) 225502.
[47] P. Dommersnes, Z. Rozynek, A. Mikkelsen, R. Castberg, K. Kjerstad, K. Hersvik, J. Otto Fossum, Nat. Commun. 4 (2013) 2066.
[48] Z. Rozynek, J. Banaszak, A. Mikkelsen, K. Khobaib, A. Magdziarz, Soft Matter 17 (2021) 4413.
[49] J.R. Melcher, G.I. Taylor, Annu. Rev. Fluid Mech. 1 (1969) 111.
[50] A. Mikkelsen, Z. Rozynek, K. Khobaib, P. Dommersnes, J.O. Fossum, Colloid Surf. A 532 (2017) 252.
[51] Z.L. Yan, C. Louste, P. Traore, H. Romat, J. Electrostat. 71 (2013) 478.
[52] A.E. Perri, A. Sankaran, C. Staszel, R.J. Schick, F. Mashayek, A.L. Yarin, Exp. Fluids 62 (2021) 27.
[53] B.W. Wagoner, P.M. Vlahovska, M.T. Harris, O.A. Basaran, J. Fluid Mech. 904 (2020) R4.
[54] Q. Brosseau, P.M. Vlahovska, Phys. Rev. Lett. 119 (2017) 034501.
[55] H. Xu, J. Wang, J. Tian, Y. Huo, B. Li, D. Wang, W. Zhang, J. Yao, Exp. Therm. Fluid Sci. 126 (2021) 110378.
[56] M. Gao, L.-S. Zhang, D. Zhang, L.-X. Zhang, Exp. Therm. Fluid Sci. 104 (2019) 9.
[57] M.T. Harris, O.A. Basaran, J. Colloid, Inteface Sci. 161 (1993) 389.
[58] M.T. Harris, O.A. Basaran, J. Colloid, Inteface Sci. 170 (1995) 308.
[59] W. Grassi, D. Testi, D. Della Vista, J. Electrost. 64 (2006) 574.
[60] W. Grassi, D. Testi, Int. Commun. Heat Mass Transf. 104 (2019) 83.